ELSEVIER

Journal of Alloys and Compounds 224 (1995) 305–315

Journal of ALLOYS AND COMPOUNDS

A surface analytical study of SO_2 stabilisation of $LaNi_5H_x$ surfaces

S. Myhra [a,b], E.H. Kisi [b,*], E.M. Gray [b]

[a] *AEA Industrial Technology, Harwell Laboratory, Harwell, Oxfordshire OX11 0RA, UK*

[b] *Faculty of Science and Technology, Griffith University, Nathan, Queensland 4111, Australia*

Received 22 April 1994; in final form 22 December 1994

Abstract

The stabilisation of $LaNi_5H_6$ by SO_2 poisoning, under conditions approximating those expected in real engineering applications of the hydride, has been investigated with several complementary techniques – SEM, TEM, XPS, XAES and in-situ XRD. The effects of hydrogen loading and SO_2 exposure, and of the ambient conditions include: the formation of a 1–2 monolayer thick oxide film at the interface between the gaseous ambient atmosphere and the solid; the formation of a 25–100 nm thick decomposition layer below the oxide film; and the retention of the alloy below the decomposition layer. The decomposition layer is found to be depleted in Ni, according to XPS analyses, while TEM reveals the presence of nano-crystallites (most likely Ni) embedded in an amorphous matrix; the latter consists of mixed oxide, hydroxide and carbonate species. The relationships between the data have resulted in the formulation of a model which proposes that the nano-crystallites promote dissociative/associative H_2 chemisorption/desorption at surface sites which under normal circumstances are protected against poisoning by the surrounding amorphous matrix, which is permeable to H_2. The effect of SO_2 exposure is apparently for the S to react at the surface sites of the nano-crystallites, to form a sulphide, thus stabilising the fully loaded hydride by prevention of associative desorption. There is little, if any, penetration by S of the metal hydride substructure. Also, we find that long-term stability is promoted by the presence of trace amounts of SO_2 in the ambient atmosphere; this suggests that the stabilisation is, at least in part, a dynamic process.

Keywords: Stabilisation; Sulphides; Metal hydrides

1. Introduction

In metal hydride storage systems, it is generally accepted (e.g. [1]) that hydrogen uptake proceeds in four stages by: (a) adsorption of H_2 onto the metal surface; (b) dissociation of H_2 molecules into chemisorbed atomic H; (c) diffusion of H into the metal to form a solid solution; and (d) formation of the concentrated hydride phase. Step (d) is absent if the system is above its critical temperature. There has been much debate in the literature about which of the steps is rate controlling in different systems and under different conditions. In addition, many metals and alloys (e.g. FeTi) which will not form hydrides in bulk air-exposed form, will readily absorb H after an activation treatment, usually consisting of exposure to H_2 at elevated temperature (200–400 °C).

Previous surface analytical studies of AB_n alloys [e.g. 2–6] have demonstrated surface oxidation of the A species and surface depletion of the B species. The depletion has often been interpreted as being due to lateral segregation and formation of B clusters which present a smaller area to a broad-beam probe (e.g. XPS). Since B is generally a transition metal species, strong catalytic activity has often ascribed to these clusters [2,4,7]. Schlapbach [8] found that cycling hydrogen into and out of $LaNi_5$ increased the magnetic susceptibility due to the precipitation of Ni-rich superparamagnetic clusters. In fact, the sample eventually became ferromagnetic. Removing the sample surface decreased the susceptibility to the value expected for pure $LaNi_5$ (a Pauli paramagnet), showing that the clusters were near the surface. Further evidence for the catalytic activity of the segregated 3-d clusters in hydrogen storage alloys has come from the study of the effect of metallic overlayers deposited on Ta [9]. It was found that Pd overlayers increased the absorption rate of Ta by four orders of magnitude, and Ni and

* Now at the Department of Mechanical Engineering, University of Newcastle, NSW 2308, Australia.

SSDI 0925-8388(95)01535-3

Fe increased the absorption rate by 10–100 times. Hence a hypothesis has arisen that, irrespective of the procedural details, the essential attribute of activation is to achieve the formation of catalytically active 3-d clusters in the surface layer of the hydride.

By contrast, there are results which contradict this view. The commonly reported activation procedure for FeTi of heating to 400 °C in H_2 corresponds to physical separation of the surface oxide layer according to [10]. In H, D "scrambling" experiments [11] it was found that FeTi is catalytically inactive at room temperature, but is activated by heating to 200 °C in H_2 and retains this activity on cooling to room temperature. It is unclear whether it was the precipitation of Fe on the alloy surface or the cracking off of an oxide layer which activated the FeTi. Pure Fe, on the other hand, became active above about 300 °C in H_2 but lost this activity on cooling, which favours the latter explanation for the behaviour of FeTi. In a subsequent study [12] TiFe overlayers on Ti films were found to have little effect, however. Ni was found to be activated below 100 °C and to remain catalytically active on cooling [11].

$LaNi_5$ requires no specific activation treatment. Surface analytical results for $LaNi_5$ conform to the trends above showing a La-enriched surface layer, present as oxide, and apparent depletion of the Ni species near the surface [3,5,6], commonly interpreted as the formation of Ni clusters, even though the composition and structure of these have not been demonstrated by unequivocal evidence.

Hydriding will not proceed if one of the four steps outlined above is blocked. If the surfaces of hydridable metals and alloys are truly catalytic, known catalytic poisons should be effective in preventing dissociation of H_2. Han and Lee studied the poisoning of $LaNi_5$ by O_2 [13] and CO [14]. Some recovery of activity was noted after one cycle in $H_2+0.1\%$ O_2 due, it was thought, to catalytic $La(OH)_3$ or Ni in the surface. Cycling in H_2+400 ppm CO resulted in a loss of H storage capacity (i.e. selective poisoning of some powder particles). This was thought to be due to the preferential adsorption of the CO molecule onto surface sites active for the dissociative chemisorption of H. In an earlier study [15], similar conclusions had been reached with respect to CO, which appeared to be a cumulative poison. $LaNi_5$ was reported to develop an immunity to O_2 poisoning, suggesting that the oxide itself may be catalytically active. Indeed in [16], $CeNi_{5-x}Co_xO_y$ ($y \sim 3.8$) was used as a catalyst for the synthesis of CH_4 from CO and H_2. It has been shown [17] that the sticking coefficient of hydrogen on Ni surfaces covered with S or O will be reduced to essentially zero from an original value of about 0.2. The sulphur was very difficult to remove (requiring 30 min at 1100 K in vacuum), suggesting that S is an effective long-term poison against absorption. Also, SO_2 has been shown to be very effective as a poison against H absorption in $LaNi_5$, $PrCo_5$, $ErCo_5$, $HoCo_3$ and $ErFe_2$ [18].

We will refer to the prevention of H desorption as stabilisation of the hydride phase. The successful stabilisation of $LaNi_5$ using SO_2 has been reported [18]. In addition, CO has been used to retard desorption during transfer of $LaNi_5H_6$ from the hydriding chamber to a vanadium can for neutron diffraction [19]. Apart from these reports, the topic of stabilisation of the hydride appears to have received relatively little attention in the existing literature.

The major objectives of the present study were threefold. Firstly, it constitutes an investigation into the surface and near-surface alterations associated with activation/passivation of $LaNi_5$ and stabilisation of $LaNi_5H_6$ under practical laboratory conditions representative of those that are likely to be operative during technical applications of the hydride. Most of the previous work has been concerned with ideal conditions, such as low exposures, extreme UHV environments and dosing with ultra-pure gases. Secondly, the intentions have been to correlate the results from surface analysis with those from XRD and pressure–temperature measurements during the activation, hydriding and stabilisation procedures. Finally, we have attempted to add to the existing body of knowledge dealing with the effects of stabilisation and poisoning of the $LaNi_5$ hydride. Again, the emphasis has been on monitoring these effects under engineering conditions.

2. Experimental details

2.1. Sample preparation

Specimen materials, with composition $LaNi_{4.93}$, from Research Chemicals (alloy #1241) were used throughout this work. Two single crystal reference samples were first prepared. These were: (a) sample SP, a $5\times3\times1$ mm^3 crystal with one side ground flat and polished with 1 μm diamond paste; (b) sample B, a $7\times3\times3$ mm^3 crystal prepared as for SP above, and then exposed to SO_2 at 270 kPa for 24 h and stored in air.

Several as-received samples were then activated for H absorption at 23 °C in a manometric hydrogenator by five adsorption/desorption cycles. Cycling was conducted stepwise by filling a reference volume to a carefully measured H_2 pressure, opening a valve to the specimen chamber and recording the pressure decrease in the total volume. At this stage, two additional reference samples were prepared; (a) sample D, which was merely an activated powder, stabilized (against auto-ignition in air) in an air/argon mixture, and (b) sample E, an activated powder exposed to 270 kPa of SO_2 for 2 h.

Preparation of fully loaded hydride samples proceeded as follows. After the completion of the fifth cycle, the samples were loaded to a H content equivalent to $LaNi_5H_6$ for a sixth time, the pressure was adjusted to 350 kPa (~100 kPa above the absorption plateau pressure at this temperature) and the sample chamber was sealed. This sealed sample chamber was then coupled to the poisoning apparatus, which was similar to the hydriding apparatus but had a source of SO_2 instead of H_2. Poisoning of the surface then proceeded in one of two ways.

(1) The sample chamber was cooled to 77 K for 40 min and the remaining gaseous H_2 pumped off (the desorption pressure at this temperature is only a few Pa, and the desorption kinetics are very slow). The sample chamber was then flooded with SO_2 at cylinder pressure (270 kPa, the pressure of the liquid–gas transformation at room temperature) for 2 min. This was followed by storage for several hours at 77 K and slow warming to room temperature by allowing the covered 2 l dewar of liquid nitrogen to boil dry and warm in air over a period of 19 h. A further 4 h period at room temperature was allowed before the specimen chamber was cleared of gaseous SO_2 and the specimen was removed in an argon-filled glove bag. Three portions of the powder sample were stored in three 4 cm^3 bottles under (a) air (sample X1), (b) argon (sample X2), and (c) SO_2/air (sample X3), for X-ray analysis.

(2) Following a procedure outlined by [18] the reference volume of the poisoning apparatus (10.7 cm^3) was evacuated at room temperature and then filled with SO_2 at 270 kPa. This SO_2 was then allowed to mix with the H_2 in the sample chamber (92 cm^3) for a few minutes. The sample was again isolated, the reference volume evacuated and the procedure repeated until the average mole fraction of SO_2 was 0.58 in the total volume. Sixteen hours were then allowed to elapse before the sample chamber was evacuated and the sample (F) divided into two portions, under argon, for XRD and surface analysis. A summary of the specimen details appears in Table 1.

2.2. SEM and TEM

A JEOL JSA 840 microprobe was used to carry out scanning electron microscopy (SEM) and microanalysis of the poisoned powders, both at the surface and in cross-section (by setting in epoxy and polishing to a 1 μm finish). This gives a view of the powder particles at depths intermediate to the essentially bulk measurements with XRD and the surface analytical measurements.

Transmission electron microscopy (TEM) was carried out on samples given many hydriding/dehydriding cycles followed by treatment in air/argon (e.g. sample D). JEOL 1200FX and JEOL 4000FX instruments were used in this work. The edges of the particles are generally thick and difficult to work with due to the high density of dislocations and the strain fields generated by the hydriding process. However, some useful images were obtained (see Section 3.1).

2.3. XRD

Powder XRD was used to monitor the proportions of the β-phase hydride in the stabilised hydride samples as a function of the time elapsed after opening of the sample bottle. No distinction is made in these analyses between the alpha phase (dilute solid solution of H in $LaNi_5$) and the $LaNi_5$ metal. Scans were recorded using Fe filtered Co Kα radiation, usually in the 2θ range 30–60°. In order to reduce the scan time and hence have a more instantaneous measure of phase proportions, some scans were carried out over a smaller 2θ range, 32 to 37°. The raw data were analysed using a Rietveld refinement program, modified to account for anisotropic broadening of the reflections [20], to provide scale factors for quantitative phase analysis [21].

2.4. XPS and XAES

The specimens were stored under argon gas in a glove box. The finely divided powder specimens were

Table 1
Specimen details

Specimen	Configuration	Treatment
SP	Single crystal	Polished, stored in air
B	Single crystal	Polished, poisoned in SO_2 for 24 h at 298 K
D	Powder	Activated (5 cycles), de-hydrided, stabilized in air/argon
E	Powder	Activated (5 cycles), de-hydrided, poisoned in SO_2 at 298 K
F	Powder	Activated (5 cycles), hydrided, poisoned in SO_2 at 298 K
X1	Powder	Activated (5 cycles), hydrided, poisoned in SO_2 at 77 K, stored in 4 cm^3 of air
X2	Powder	Activated (5 cycles), hydrided, poisoned in SO_2 at 77 K, stored in 4 cm^3 of argon
X3	Powder	Activated (5 cycles), hydrided, poisoned in SO_2 at 77 K, stored in 4 cm^3 of SO_2/air mixture

mounted on a copper-backed tape and transferred under vacuum to the spectrometer chamber. X-ray photoelectron spectroscopy (XPS) and X-ray (induced) Auger electron spectroscopy (XAES) analyses were carried out in a VG ESCALAB Mark II instrument. The Al Kα line was used as the exciting radiation at a source power of 250 W. Survey scans were obtained over a kinetic energy range of 400–1500 eV. The major peaks were scanned repetitively in order to improve the signal-to-noise ratios in steps of 0.2 eV with a pass energy (CAE) of 25 eV. Minor charge shifts were corrected by referencing to the graphite C 1s binding energy of 284.8 eV. Sequential ion beam bombardments were used to profile into the as-received surfaces; a 3 kV argon ion beam was used, rastered over 1 cm^2, and with current densities ranging from 1 to 10 $\mu A\ cm^{-2}$. High-purity Ar gas (<1 ppm impurities) was fed to a Leybold ion gun during this procedure, and the beam was rastered over the specimen area. Previous experience and calibration on Ta_2O_5 films suggest that the rate of erosion was approximately 0.2 nm per 1 μA min cm^{-2} of ion dose (ΣD). A standard software package and empirical sensitivity factors were used to quantify the results. Because of the interference between the Ni 2p and La 3d regions the sensitivity factors were adjusted in order to base the quantifications on the Ni $2p_{1/2}$ and La $3d_{5/2}$ peak areas. A three-point smoothing routine was used to improve the shapes of some low-intensity peaks. A Shirley-type background was subtracted from the detailed scans.

3. Results

3.1. SEM and TEM

A typical image of a few sectioned powder particles of sample X3 is shown in Fig. 1(a). Note the large number of highly branched cracks and the rough exterior surface of the particles due to the hydriding treatment. There were no observable changes in morphology as a result of stabilisation by SO_2. Microprobe analysis of the regions more than 0.5 μm from the cracks (i.e. the bulk) showed only La and Ni in the correct molar proportions (Fig. 1(b)). However, when the electron beam was focused onto a crack, an easily detected sulphur signal was excited (Fig. 1(c)). Although the crack and beam spread in the sample preclude assigning quantitative significance to the resulting analyses, it nevertheless shows that substantial amounts of S are retained in the near-surface regions. Measurements on other samples treated with SO_2, and on the same samples viewed from the exterior of the particles (unsectioned), gave similar results. The sulphur signal, as monitored by EDXS, persisted for the duration of the project (in excess of one year).

Typical examples of TEM images obtained from activated powders (subjected to brief air exposure during transfer) are shown in the dark-field/bright-field image pair (Fig. 2). Similar results have been obtained in other studies [22]. There is clear evidence of an altered layer at the particle surface, particularly in the dark-field image. Because the specimen edge was shaped like a blunt wedge, the true thickness of the layer could not be measured but it appeared to be of order 10 nm in this image and up to 40 nm in others. Note that many nano-crystals in the layer gave strong diffraction at the chosen dark tilt setting of [110].

3.2. XRD

A portion of sample X1 was placed in the X-ray diffractometer after storage for 1 h in air in a small container. A 30 min scan showed it to be 100% β-phase, consistent with stabilisation on this time scale. The same sample was left overnight in the diffractometer (in essentially an infinite amount of air); during this period the hydrogen desorbed completely. The remaining portion of X1 was stored overnight in air in a closed sample bottle; this also exhibited total loss of hydrogen.

Sample X2, stored in 4 cm^3 of Ar/air mixture, remained 100% β-phase after 18 h. After 2.5 h in the XRD chamber, it had outgassed to be 75% β-phase, and after a further 2 h it was down to a 50% volume fraction. Monitoring was then discontinued.

Sample X3, stored in 4 cm^3 SO_2/Ar/air, remained 100% β-phase after 4 days in the sample container. The progressive hydrogen loss was then monitored for a further 2 days and quantified using Rietveld analysis and standard quantitative phase analysis techniques [21]. Fig. 3 shows a typical two-phase XRD pattern and Rietveld analysis. Clearly the statistical noise was greater than ideal, because scan times longer than 30 min were impractical for recording a dynamic process.

3.3. XPS and XAES

3.3.1. General observations and data overview

The interference between the Ni $2p_{3/2}$and La $3d_{3/2}$ features, which is exacerbated by contributions from various satellite structures, imposes not only the need to base quantification on the generally well-resolved Ni $2p_{1/2}$ and La $3d_{5/2}$ components, but also the need to infer chemical information from the binding energies of these lines.

Correlations between the quantified results from single crystal and powder specimens need to be treated with some caution. The results from the latter configuration must of necessity refer to irregularly shaped powder particles with facets at random orientations *vis-à-vis* the incident ion beam, and averaged over all

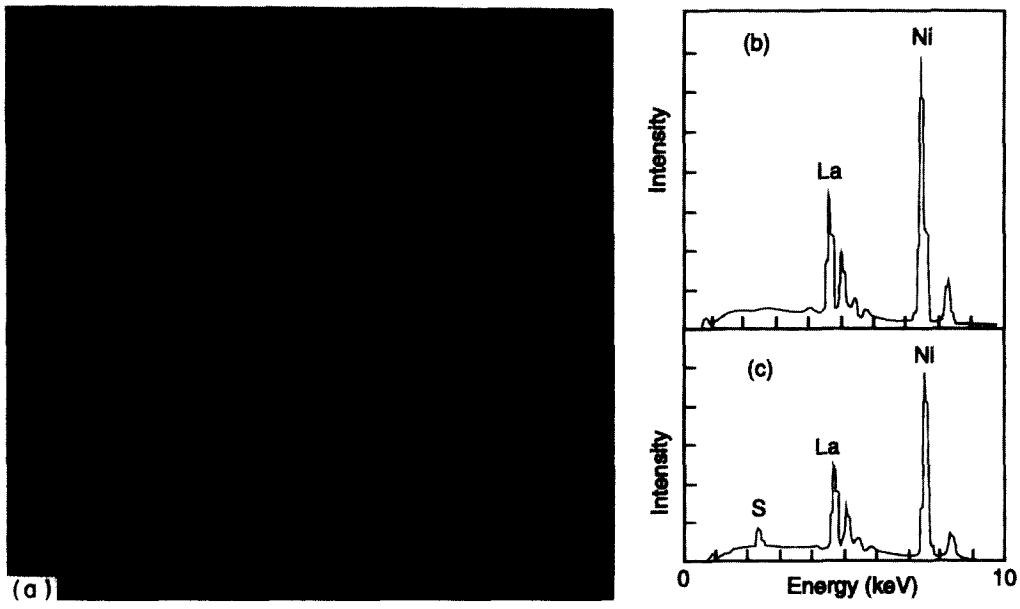

Fig. 1. (a) Secondary electron image of sample X3 sectioned powder showing extensive cracking. The magnification bar is 10 μm. EDXS spectra show (b) the sulphur-free bulk and (c) sulphur-enriched crack regions.

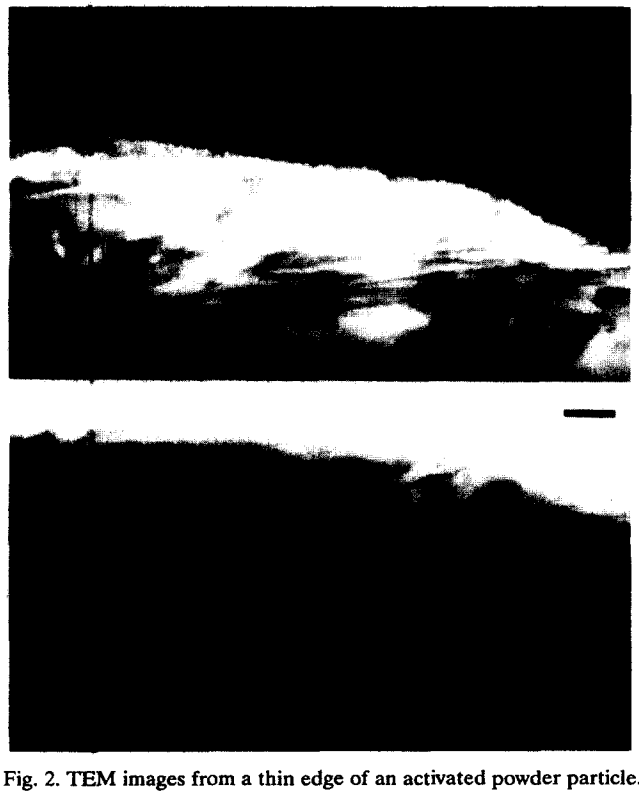

Fig. 2. TEM images from a thin edge of an activated powder particle. A [110] dark field and bright field image are shown. The bar is 50 nm.

take-off angles. The depth profiles for the powder specimens therefore are representative of information from varying depths below the original as-received surfaces. Specimens D, E, F and X3 were subjected to identical activation and hydriding/dehydriding treatments. Since XPS/XAES are broad-beam techniques the lateral averaging will ensure that major differences in the results for these specimens are significant, rather than being geometrical artefacts. However, it is likely that the depth dependences will have been broadened out over a greater depth range, in comparison with the results obtained from the single-crystal specimens.

Base vacuum in the spectrometer chamber typically was better than 10^{-9} Torr, although the vacuum deteriorated after the powder specimens were introduced, due to outgassing from the large surface areas of the micro-fractured specimens. The La species is extremely reactive, and will therefore be detected as oxide or hydroxide, irrespective of its chemical state in the metal alloy. On the other hand, Ni is considerably less reactive; the observed chemical state(s) is/are therefore more likely to be representative of the chemical environment in the hydride alloy.

A number of representative detailed scans over the Ni 2p/La 3d region are shown in the montage in Fig. 4. The emphasis has been placed on results from as-received surfaces and from the transition regions in the depth profiles, for low values of Ni/La.

The evolution of the Ni/La ratio with depth, but shown as ion dose, below the original surface for specimens SP, B, E, F and X3 is plotted in Fig. 5. The sulphur abundances, quantified on the assumption that Ni+La+S=100%, as functions of ion dose are shown for the "poisoned" specimens in Fig. 6. The kinetic energies K.E. of the Ni LMM maxima and the binding energies B.E. of the Ni $2p_{1/2}$ peaks are plotted in Fig. 7 as functions of ion dose for the relevant specimens. There is a similar plot for the La $3d_{5/2}$ and S 2p binding energies in Fig. 8. In the case of the latter species the high-B.E. (sulphate-like) component

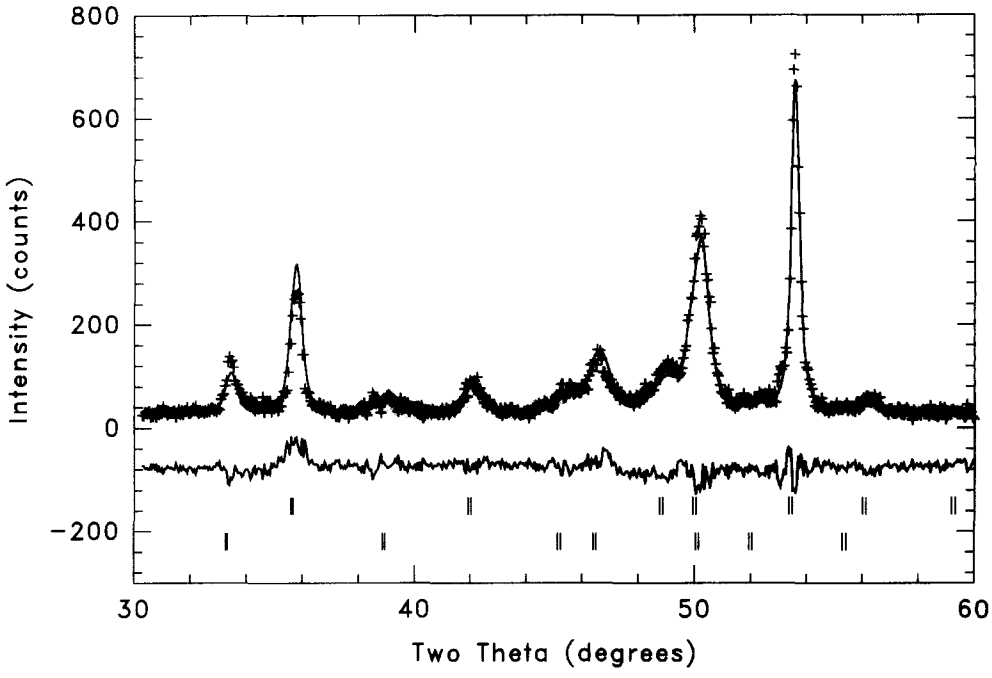

Fig. 3. Rietveld fit to X-ray diffraction scan of sample X3 after 4 days' storage in 4 cm^3 of SO_2/Ar/air mixture followed by 22 h in the XRD chamber. The data are shown by (+), the calculated profile as a solid line and their difference as a solid line below the main figure. Short vertical bars show the peak positions for both phases.

is distinguished from the low-B.E. (sulphide-like) component; the shapes and positions of representative S 2p signals are illustrated in Fig. 9. The signal-to-noise ratios were relatively poor for these spectra due to low abundances and low sensitivity factors. Finally, the binding energies of the major contributions to the O 1s envelopes are found in Fig. 10 as functions of ion dose. The low-B.E. entries, in the range 529.0–530.5 eV, are representative of oxides, while the high-B.E. line, in the range 531.0–532.5 eV, is likely to represent hydroxides. The data points above 533 eV for the B specimen suggest the presence of carbonate. The relative contributions of high-B.E. and low-B.E. species to the oxygen abundances, A_H/A_L, for several specimens are shown in Fig. 11; hydroxide contributions are relatively more prominent for $\Sigma D < 20$, as expected.

As an aid to the discussion below, selected results and data from the literature [5,6,23] for binding and kinetic energies have been collated in Table 2. Also, for purposes of facilitating detailed discussion we will provide a brief summary of the main features of the results for each specimen.

3.3.2. Polished single crystal (SP)

This specimen exhibited a thin, somewhat Ni-rich, oxide layer on the as-received surface. This oxide layer was removed by a light sputter etch, below which was found a Ni-depleted layer. Additional ion beam erosion returned the Ni/La ratio to near-normal stoichiometry. Evidence was found for hydroxide and carbonate species.

3.3.3. Poisoned single crystal (B)

As well as adventitious carbon and physi- and chemisorbed O_2 and CO_2, SO_2-like and sulphate species were found in the as-received surface. Most of these constituents were removed by a light ion beam dose, $\Sigma D = 2.5$, after which mainly sulphide-like species were predominant. Oxides made some contribution to the Ni 2p envelope, and were major features of the La 3d envelope. Some hydroxide and carbonate formation was also evident (i.e. O 1s components at 531–532 and 533–534 eV). The thickness of the sulphur bearing layer only extended to a depth equivalent to $\Sigma D \approx 10$, allowing for some variation in the rate of erosion across the surface, but the relative contributions from hydroxides/carbonates persisted and increased to a dose of at least $\Sigma D = 37.5$, at which point the profiling was terminated.

3.3.4. Activated powder specimen (D)

The compositional results for this specimen were deemed to be unreliable, due to possible non-standard alignment of the ion gun *vis-à-vis* the specimen surface. The kinetic/binding energies obtained from profiling suggested, however, that the as-received surface was oxidized, but that there were few, if any, contributions from hydroxides.

3.3.5. Activated and poisoned powder specimen (E)

This specimen exhibited an intermediate value for the Ni/La ratio in the as-received surface. Beyond this there was a substantially Ni-depleted region (Ni/La $\approx$ 1), followed by a trend towards the nominal stoichiometry.

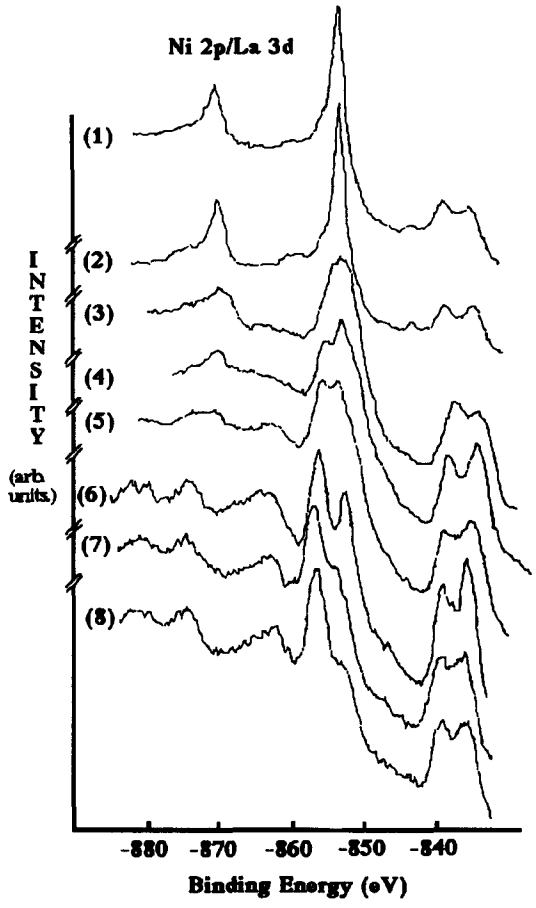

Fig. 4. Representative scans over the Ni 2p/La 3d region. The sequence illustrates typical chemical information from clean alloy surfaces following removal of altered surface layers (curves 1 and 2), various locations in the Ni-depleted layer (curves 3, 4 and 5), and for several as-received surfaces (curves 6, 7 and 8). The scans refer to the following specimens and surface conditions: (1) specimen E and $\Sigma D = 77.5$; (2) specimen B and $\Sigma D = 37.5$; (3) specimen X3 and $\Sigma D = 37.5$; (4) specimen F and $\Sigma D = 17.5$; (5) specimen E and $\Sigma D = 7.5$; (6) specimen F and $\Sigma D = 0$; (7) specimen X3 and $\Sigma D = 0$; (8) specimen E and $\Sigma D = 0$.

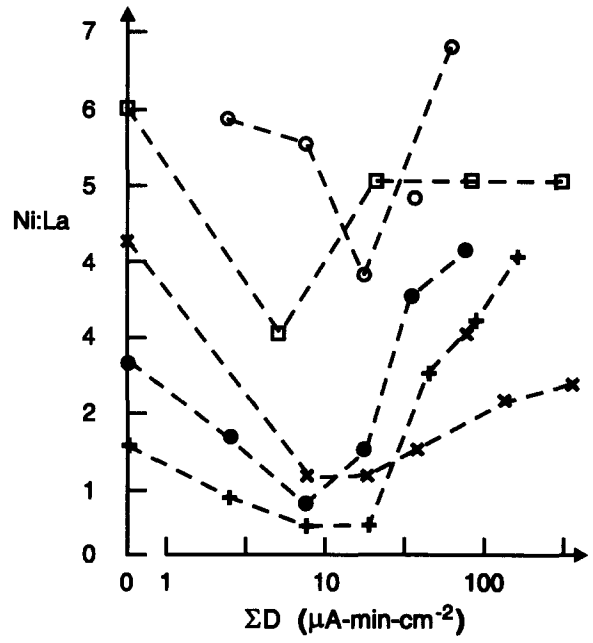

Fig. 5. The ratio of Ni to La abundance as a function of ion beam dose for representative specimens. The key to the symbols in this diagram, and subsequent Figs. 6–11 is: X3 (×), E (●), F (+), B (○), D (□).

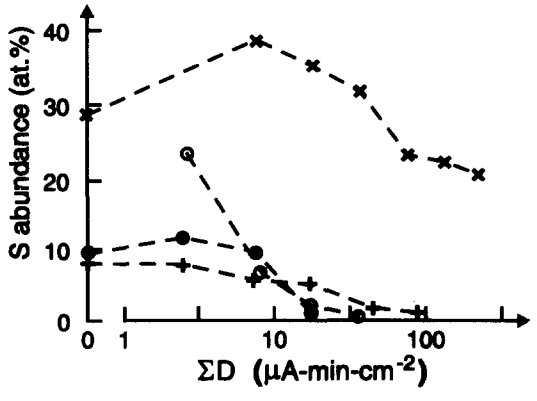

Fig. 6. The abundance of S in the surface layers of poisoned/stabilised specimens. Quantification of S was carried out on the assumption that La + Ni + S = 100%. No distinction was made between S in different chemical states. See Fig. 5 for key to symbols.

The presence of S amounted to approximately 10 at.% to a depth equivalent to $\Sigma D \approx 10$; beyond this depth the S abundance dropped to the level of detectability at $\Sigma D \approx 20$. Hydroxylation of both La and Ni species was evident for $\Sigma D < 10$. Beyond this depth La-oxide and mixed Ni/Ni-oxide were predominant.

3.3.6. Activated, hydrided and poisoned (298 K) powder (F)

This specimen exhibited the greatest depletion of Ni in the surface, to a depth equivalent to $\Sigma D \approx 20$, followed by a relatively rapid rise in the Ni/La ratio towards normal stoichiometry. The presence of S was modest (≈ 7 at.%), and coincided with the Ni-depleted layer. The as-received surface was dominated by hydroxides/oxides of Ni and La, to a depth equivalent to $\Sigma D = 5$–10.

3.3.7. Activated, hydrided and poisoned (77 K) powder (X3)

There was a relatively Ni-rich hydroxide/oxide layer in the as-received surface, as compared with specimen F. However, the Ni-depleted region persisted to a greater depth, and the Ni/La ratio did not recover above a value of 2.5 at the highest ion dose ($\Sigma D = 225$). The abundance of S exceeded those of specimens E and F by a factor of 3–4, and this abundance persisted to the highest etching dose into the Ni-depleted region. The chemical states of Ni and La as functions of depth were similar to those for E and F, however. Conversely, the contributions of high binding energy oxygen species persisted to a greater depth than for any other specimen,

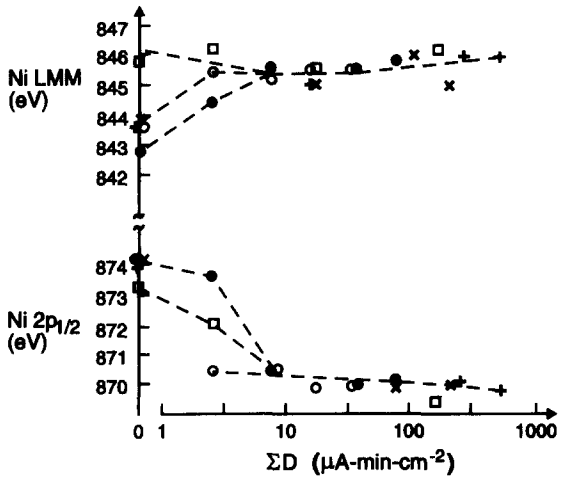

Fig. 7. The kinetic energies corresponding to the maximum intensity of the Ni LMM feature (top) and the binding energies of the Ni $2p_{1/2}$ peak (below) are shown as functions of ion dose. See Fig. 5 for key to symbols.

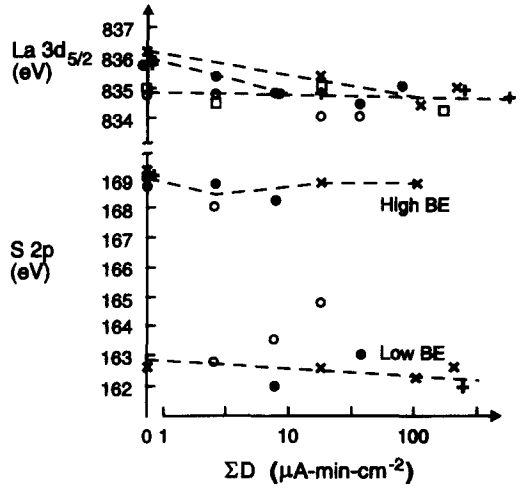

Fig. 8. The binding energies of the La $3d_{5/2}$ component as functions of ion dose are plotted (top). Likewise, the S 2p binding energies are shown as functions of ion dose. See Fig. 5 for key to symbols.

indicating a greater extent of hydroxylation in the near-surface layers.

4. Discussion

A plot of the amount of β-phase hydride against time in the XRD chamber is given in Fig. 12 (solid circles). The line is a fit to the Johnston–Mehl–Avrami equation

$$\%\beta = 100 \exp\{-[k(t-t_0)]^n\}$$

The best fit obtained for sample X3, Fig. 12 (open circles), corresponded to $n = 1.00$: consistent with exponential decay, and indicative of first-order kinetics. Sample XF gave $n = 1.57$ and considerably faster kinetics. We interpret these data as indicating that in XF, the

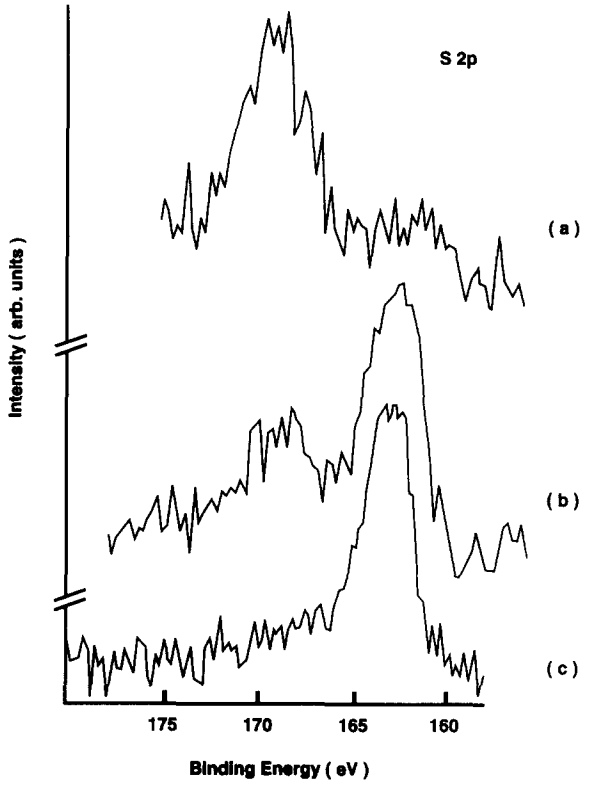

Fig. 9. Representative spectra for the S 2p structure. The sequence shows: (a) high binding energy species in the as-received poisoned surface; (b) high and low binding energy species after removal of a few monolayers ($\Sigma D = 2.5$); and (c) exclusively sulphide-like species in the decomposition layer ($\Sigma D = 7.5$). These results were obtained for specimen B. The data have not been smoothed.

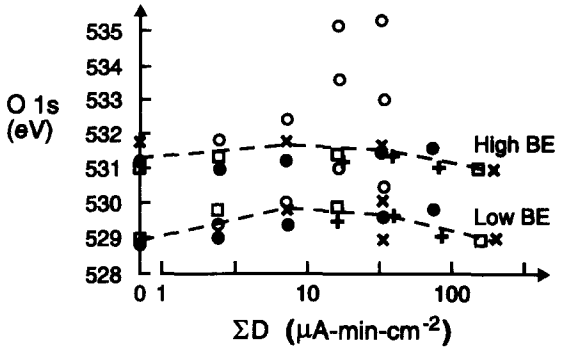

Fig. 10. The binding energies of the main components of the O 1s structures are shown as functions of ion dose. See Fig. 5 for key to symbols.

degassing kinetics are convoluted with those of H desorption, but in X3, the rate limiting process is degassing of the poison. The first-order kinetics for X3 suggests that for this sample SO_2 is adsorbed without dissociation, according to the equilibrium Langmuir isotherm

$$SO_2(g) \longleftrightarrow SO_2(ads)$$

$$\theta = \frac{(k_{ads}/k_{des})P}{1 + (k_{ads}/k_{des})P}$$

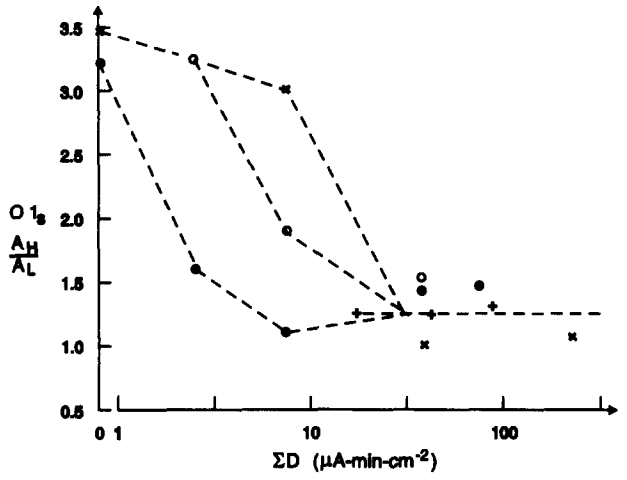

Fig. 11. The relative contributions of high and low binding energy species (A_H/A_L) to the O 1s structures as functions of ion dose. Only representative data are shown. See Fig. 5 for key to symbols.

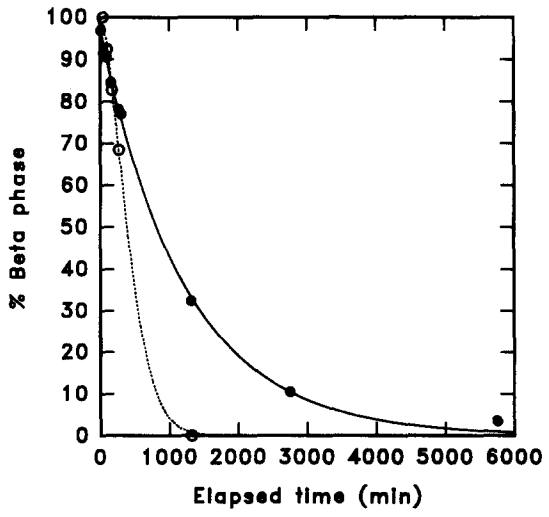

Fig. 12. Change in phase proportions in samples X3 (●) and F (○) with time in the X-ray chamber. The fitted lines represent calculations using the JMA equation for diffusion-controlled processes.

Table 2
XPS/XAES data: binding/kinetic energies from the literature

Compound	Level	Energy (eV)	Comments [a]	Ref.
La	La $3d_{5/2}$	835.8	Sat. at 843.0	[5]
La_2O_3	La $3d_{5/2}$	834.8	Sat. at 839.1	[5]
$La(OH)_3$	La $3d_{5/2}$	836.0	Sat. at 839.8	[5]
La_2O_3	O 1s	530.2		[6]
$La(OH)_3$	O 1s	532.2		[6]
Ni	Ni $2p_{1/2}$	870.2	Sat. at 858. 4	[5]
NiO	Ni $2p_{1/2}$	873.1	Sat. at 861.8	[5]
Ni_2O_3	Ni $2p_{1/2}$	872.7	Sat. at 862.4	[5]
$Ni(OH)_2$	Ni $2p_{1/2}$	874.2		[5]
NiO	O 1s	529.7		[6]
$Ni(OH)_2$	O 1s	531.4		[6]
Ni	Ni LMM	846.5		[5]
NiO	Ni LMM	846.2		[5]
Ni_2O_3	Ni LMM	844.5		[5]
$Ni(OH)_2$	Ni LMM	841.9		[5]
NiS	S 2p	162.8		[23]
S(elemental)	S 2p	164.3		[23]
SO_2	S 2p	167.4		[23]
$CuSO_4$	S 2p	169.1		[23]

[a] Sat. refers to satellite structure.

where k_{ads} and k_{des} are the rate constants for adsorption and desorption. The stabilisation of sample XF against hydrogen loss in air may have failed completely, since the measured kinetics of the reversion to the β-phase could feasibly be that of the unpoisoned material.

From our results it would appear that SO_2 is a "dynamic" poison, requiring a surrounding SO_2 atmosphere to maintain an adequate surface coverage. This contradicts the results in [18], where SO_2 is claimed to be a "static" poison.

The present surface analysis results show that there are several microstructural, compositional and chemical effects of stabilising and hydriding $LaNi_5$. We find a thin, 1–2 monolayer surface oxide layer on all specimens. Below the surface oxide layer, there is a "decomposition" layer of variable thickness, 25–100 monolayers. At greater depths is found the bulk alloy.

Structural analysis by TEM after one or more hydrogen loading/unloading cycles shows that the bulk alloy is extensively strained and defected, while the decomposition layer consists of crystallites, with size of order nm, embedded in amorphous material [22]. Compositional analysis by XPS shows that the decomposition layer is Ni-depleted, with Ni/La in the range 0.5–3. The surface oxide skin, on the other hand, is Ni-rich. The sulphur abundances are high in the oxide skin, and persist through the decomposition layer, before decreasing to the limit of detectability at or near the interface with the bulk alloy. It should be noted that the XPS quantification of the thin oxide skin, using routine numerical procedures, will understate the extent of Ni enrichment, since the thickness of the interaction volume (as defined by the elastic mean free path) exceeds the layer thickness.

The chemical states of species as functions of depth are revealed by the details of the XPS spectra. The thin surface film consists predominantly of oxidized matrix species, while the sulphur is present as tetravalent sulphate-like species. In the decomposition layer, we find a mixture of oxides, hydroxide and metallic species, as well as some carbonate. La persists as an oxide even in UHV conditions, presumably due to the extreme reactivity of this species. On the other hand, Ni increasingly acquires a metallic signature with depth, even in the decomposition layer. This is consistent with previous inferences from surface analytical investigations [3,5,6], and from TEM investigations [20], which are consistent with crystalline clusters co-existing with

other phases in this layer. Finally, the sulphur occurs as sulphide-like species in this layer.

The present investigations were carried out on specimens and surfaces which had been subjected to realistic "laboratory" conditions during preparation, hydriding and stabilisation. These conditions are relatively "dirty" in comparison with those that pertain to many, if not all, of the previous surface analytical investigations of $LaNi_5$. Most of these investigations have focused on changes in the surface reactivities of the original "free" surfaces due to relatively modest dosing with various gaseous poisons. Thus the effects on catalytic properties of clean and poisoned surfaces have been of paramount interest, and have been correlated with a number of kinetic and thermodynamic regimes. While many of these observations are of intrinsic merit, they may not be relevant to the interpretation of the present experiments.

The general trends in the stability of the fully loaded $LaNi_5H_6$ hydride have been summarised in Table 3. At ambient temperature, it can be seen that an unstabilised fully loaded β-phase hydride specimen will revert to the α-phase within a short time; XRD suggests a time constant of minutes, but it may be shorter. Stabilisation with SO_2 will extend the lifetime to hours in vacuum. This can be further extended by storing the β-phase specimen in an atmosphere containing traces of SO_2. The latter observation gives additional credence to the notion that sulphur is a dynamic poison.

The clusters in the decomposition layer merit special consideration in view of their apparent significance for the hydriding, poisoning and stabilisation of $LaNi_5$. These clusters are clearly visible in the TEM images in Fig. 2, which also show the extent of the decomposition layer. The dark-field image, in particular, shows that the clusters are crystalline, and are embedded in an amorphous matrix. However, the clusters are too small for direct structural and compositional analyses by routine methods. Instead we have to fall back on indirect evidence. The depletion of Ni in this layer inferred from broad-beam surface analysis (e.g. XPS) is consistent with lateral segregation of this species (there is no evidence for significant segregation with depth). More convincing evidence comes from a small-angle neutron scattering study, with and without a magnetic field [24]. This study established that cycling in hydrogen of the $LaNi_5$ alloy was associated with the formation of supermagnetic clusters with radii of gyration greater than 10 nm. The weight of evidence therefore favours these clusters being Ni, and thus providing large catalytically active surfaces.

Table 3
Stability of $LaNi_5H_6$

Stabilisation	Ambient	Time constant
No	Vacuum	< Minutes
No	Air/argon	< Minutes
Yes	Argon/SO_2	Indefinitely
Yes	Air/argon/SO_2	Hours–days
Yes	Vacuum	Hours

The major new feature of the hydride/ambient system to be explored in this study, is the decomposition layer which has a thickness 25–100 monolayers and forms a continuous envelope for the bulk material. The finely dispersed nano-crystallites of Ni found in this layer appear to provide a catalytic substrate with a high specific surface area, thus promoting dissociation of incident H_2 molecules. Moreover, the nano-crystallites being embedded in an amorphous and highly reactive matrix (excess La) are readily accessible to hydrogen, while at the same time being protected against poisoning. Most of the adventitious containment species present under actual engineering conditions, such as O_2, CO_2 and water vapour, will preferentially be immobilized in the amorphous matrix, as shown by the prevalence of oxides, hydroxides, carbonates and reduced carbon in the decomposition layer.

Elevation of the nano-crystallites in the decomposition layer to prominence may also account for the effects of SO_2. Our hypothesis is that the surfaces of the Ni crystallites are the principal destinations for the sulphur. Accordingly, one should expect a sulphide XPS signature, as in NiS [23], as well as suppression of catalytic activity. The latter will effectively poison the specimen and prevent hydriding at the dissociative chemisorption stage. Likewise, it will stabilise a fully loaded specimen and prevent dehydriding at the stage of associative desorption. The full structure of an activated and stabilised $LaNi_5$ hydride is shown schematically in Fig. 13.

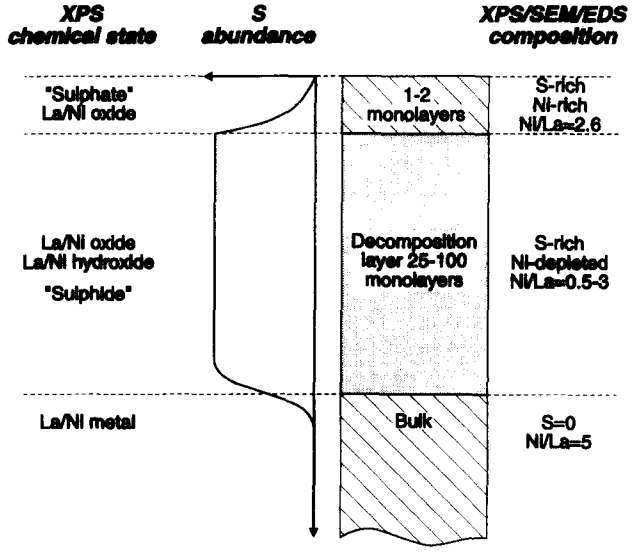

Fig. 13. Schematic representation of the surface layer structures and composition of stabilised and hydrided $LaNi_5$.

Accordingly, the observed relatively low (~5–10 at.%) abundance of sulphur in the decomposition layer is consistent with it being present as a coating on the Ni nano-crystallites. A rough calculation suggests that a nano-crystallite of average size is a cluster of 100 atoms. Assuming a spherical shape, there will be approximately 50 surface sites per crystallite; thus 50 sulphur atoms will fully passivate one crystallite, assuming that all sites are catalytically active. If 30% of the volume of the decomposition layer is filled by nano-crystallites, we find that 10 at.% of sulphur will be sufficient for stabilisation.

The present results suggest that partial stabilisation is provided at the completion of hydriding by exposure to SO_2, which presumably can access the nano-crystallites and passivate their reactive surfaces by dissociative chemisorption. Additional stability is obtained by having trace levels of SO_2 in the ambient atmosphere. This observation may indicate that sulphide species are relatively weakly bound at the catalytically active surface sites, although strongly bound as sulphate elsewhere in the decomposition layer, so there will be loss of stability over time. Maintaining a dynamic equilibrium coverage can be promoted by having traces of sulphur in the ambient atmosphere.

Acknowledgements

The present work was funded in part by the Australian Research Council. One of the authors wishes to acknowledge hospitality and assistance extended during a period of attachment to the Harwell Laboratory. Many members of the hydride research group made valuable contributions to the project.

References

[1] T.B. Flanagan, in A.F. Andresen and A.J. Maeland (eds.), *Hydrides for Energy Storage, Proc. Int. Symp. Geilo, 1977*, Pergamon Press, 1978, pp. 135–150.
[2] L. Schlapbach, *J. Less-Common Met., 89* (1983) 37.
[3] L. Schlapbach, A. Seiler, F. Stucki and H.C. Siegman, *J. Less-Common Met., 73* (1980) 145.
[4] J.H. Sanders and B.J. Tatarchuk, *J. Less-Common Met., 147* (1989) 277.
[5] P. Selvam, B. Viswanathan, C.S. Swamy and V. Srinivasan, *Int. J. Hydrogen Energy, 16* (1991) 23.
[6] P. Selvam, B. Viswanathan, C.S. Swamy and V. Srinivasan, *J. Less-Common Met., 163* (1990) 89.
[7] H.Y. Zhu, C.P. Chen, Y.Q. Lei, J. Wu and Q.D. Wang, *J. Less-Common Met., 172–174* (1991) 873.
[8] L. Schlapbach, *J. Phys. F Met. Phys., 10* (1980) 2477.
[9] K. Nakamura, H. Uchida and E. Fromm, *J. Less-Common Met., 80* (1981) 19.
[10] C.S. Pande, M.A. Pick and R.L. Sabatini, *Scr. Metall., 14* (1980) 899.
[11] P.S. Rudman, *J. Less-Common Met., 89* (1983) 93.
[12] E. Fromm and H. Uchida, *J. Less-Common Met., 131* (1987) 1.
[13] J.I. Han and J.Y. Lee, *J. Less-Common Met., 152* (1989) 328.
[14] J.I. Han and J.Y. Lee, *J. Less-Common Met., 152* (1989) 319.
[15] G.D. Sandrock and P.D. Goodell, *J. Less-Common Met., 73* (1980) 161.
[16] J.E. France and W.E. Wallace, *Lanthanide Actinide Res., 2* (1988) 165.
[17] K.D. Rendulic and A. Winkler, *Surf. Sci., 74* (1978) 318.
[18] D.M. Gualtieri, K.S.V. Narasimhan and T. Takeshita, *J. Appl. Phys., 47* (1976) 3432.
[19] P. Thompson, J.J. Reilly, L.M. Corliss, J.M. Hastings and R. Hempelmann, *J. Phys. F Met. Phys., 16* (1986) 675.
[20] E.H. Kisi, C.E. Buckley and E.M. Gray, *J. Alloys Comp., 185* (1992) 369.
[21] R.J. Hill and C.J. Howard, *J. Appl. Crystallogr., 20* (1987) 467.
[22] G.H. Kim, C.H. Chun, S.G. Lee and J.Y. Lee, *Scr. Met., 29* (1993) 485.
[23] D. Briggs and M.P. Seah (eds.), *Practical Surface Analysis*, Wiley, Chichester, 1983.
[24] E.M. Gray, *Mater. Sci. For., 27/28* (1988) 433.